

Low-Temperature Energy Transfer via Self-Trapped Excitons in Mn²⁺-Doped 2D Organometal Halide Perovskites

Som Sarang, William Delmas, Sara Bonabi Naghadeh, Vivien Cherrette, Jin Z. Zhang,* and Sayantani Ghosh*



Cite This: *J. Phys. Chem. Lett.* 2020, 11, 10368–10374



Read Online

ACCESS |



Metrics & More

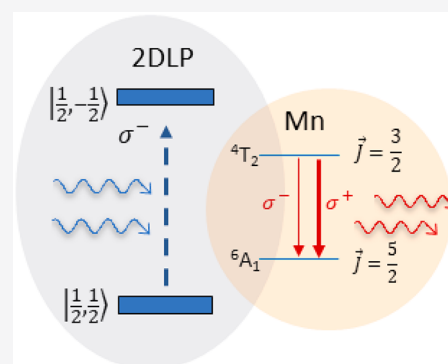


Article Recommendations



Supporting Information

ABSTRACT: We investigate the mechanisms of energy transfer in Mn²⁺-doped ethylammonium lead bromide (EA₂PbBr₄:Mn²⁺), a two-dimensional layered perovskite (2DLP), using cryogenic optical spectroscopy. At temperature $T > 120$ K, photoluminescence (PL) is dominated by emission from Mn²⁺, with complete suppression of band edge (BE) emission and self-trapped exciton (STE) emission. However, for $T < 120$ K, in addition to Mn²⁺ emission, PL is observed from BE and STEs. Data further reveal that for $20 \text{ K} < T < 120 \text{ K}$, STEs form the most dominant routes in assisting energy transfer (ET) from 2DLP to Mn²⁺ dopants. However, at higher Mn²⁺ concentration, higher activation energies indicate defect states come into play, successfully competing with STEs for ET both from BE to STE states and from STE to Mn²⁺. Finally, using polarization-resolved spectroscopy, we demonstrate optical spin orientation of the Mn²⁺ ions via ET from 2DLP excitons at zero magnetic field. Our results reveal fundamental insights on the interactions between quantum confined charge carriers and dopants in organometal halide perovskites.



The past decade has seen organometal halide perovskites (OMHPs) emerge as one of the most promising candidates for high-efficiency, lightweight, inexpensive, and scalable optoelectronic applications.¹ Among these, OMHP-based photovoltaics have proven most successful, having demonstrated a meteoric rise in power conversion efficiency in a few years to reach a value above 25%.² Other applications where OMHPs have demonstrated promising results include photodetection,³ lasing,^{4,5} light emission,^{6,7} and water-splitting.⁸ The emergence of low-dimensional variants of OMHPs have further increased the versatility of this family of compounds. For example, zero-dimensional perovskite quantum dots (PQDs) allow size-tunability of optoelectronic properties^{9–11} and demonstrate high photoluminescent quantum yields (~80%),¹² which make them strong candidates for room-temperature high-fidelity single-photon emission sources.^{13,14}

Two-dimensional layered perovskites (2DLPs) are a more recent class of OMHPs that have attracted strong interest.^{15,16} A typical 2DLP crystal structure can be described by L₂A_nX_{3n+1} where L is an organic component, A a metal cation, and X a halide anion. The metal-halide octahedra are arranged in planes forming layered planes, with the organic molecules acting as spacers in between. n denotes the number of layers that are sandwiched between the organic molecules, and their hydrophobicity has been identified as the cause of superior environmental and moisture stability in 2DLPs. 2DLPs have additionally demonstrated improved optoelectronic properties compared to their 3D counterparts, which include high

photoluminescence quantum yield (PLQY), attributed to their higher exciton binding energies due to stronger quantum confinement. This in turn leads to the formation of stable excitons at room temperature, making 2DLPs suitable candidates for light-emitting diodes (LEDs), lasing, and polariton applications.¹⁷ Both exciton binding energy and bandgap can be tuned by varying n .¹⁸ Another interesting aspect is the presence of self-trapped excitons (STEs) in 2DLPs.^{19,20} Large exciton binding energies and strong exciton–phonon coupling promote lattice distortions leading to the formation of these states that exist within the bandgap. Energy-transfer pathways allow photoexcited states to undergo fast relaxation to ensembles of STEs, resulting in broadband emission in the visible spectrum with possible applications in wide band light sources, such as white light LEDs.¹⁸

Doping in 2DLPs, specifically substituting Mn²⁺ for Pb²⁺ in the octahedra, results in further improvements to their optoelectronic properties.^{21,22} The strong interactions between the quantum confined host carriers and the dopants lead to efficient energy transfer (ET)²³ and increased PLQY, at both the band edge and the visible region through Mn²⁺

Received: November 2, 2020

Accepted: November 20, 2020

emission,^{24,25} setting the stage for high-efficiency, dual colored LEDs.^{26,27} Despite these improved qualities, the underlying ET mechanisms are not completely understood, although various routes have been proposed, including transfers assisted through STEs,²³ defect-related trap states within the bandgap,²⁸ and hot excitons.²⁹ In particular, doping Mn²⁺ into 2D single-layered (CH₃CH₂NH₃)₂PbBr₄ can lead to complete quenching of the STEs emission, attributed to efficient exciton trapping by induced shallow defects, leading to very high PLQY of Mn²⁺ dopant (78%), with an activation energy between trap states and Mn²⁺ d states calculated to be ~9.8 meV.²⁸ Insights into the roles played by these competitive ET pathways will pave the way for improved material design, thus enhancing light emission properties. They may also provide new avenues of research, such as optically manipulated magnetization^{30–34} as observed in Mn-doped II–VI nanostructures.

In this work we study Mn²⁺-doped ethylammonium lead bromide (EA₂PbBr₄:Mn²⁺) to investigate the role of STEs in host-to-dopant ET in the temperature range 20–100 K. We selectively focus on this regime because even though activation energies of various ET pathways have been extrapolated to be approximately a few millielectronvolts,²⁸ measurements have largely been carried out above their corresponding thermal scale. Consistent with previous reports, we confirm that for temperature $T > 120$ K, PL consists of only Mn²⁺ emission.²⁹ However, for $T < 120$ K, we observe the 2DLP excitonic emission, as well as the STE emission, accompanied by reduced Mn²⁺ PL, indicating a complex pathway different from the ones previously reported, dominated by ET from 2DLP to Mn²⁺ dopants via STEs. This process involves a very low potential barrier, whose magnitude is dependent on the doping concentration, and at higher Mn²⁺ concentration, higher activation energies indicate defect states come into play, successfully competing with STEs for ET both from the band edge to STE states and from STE to Mn²⁺.

We have studied an undoped and doped 2DLPs with two different concentrations of Mn²⁺ (2% and 7%), where the doping concentrations were determined using an inductively coupled optical emissions spectrometer (ICP-OES, Supporting Information, Table 1). Powder X-ray diffraction is used to

Table 1. Activation Energies of Different ET Pathways for the 2% and 7% Doped 2DLPs

doping concentration	ΔE_1 (meV)	ΔE_2 (meV)	ΔE_3 (meV)
2%	8.8	39	4
7%	12	31	2

confirm the structural evidence of the host and doped host system (Figure S1), which is consistent with a previous report.²⁸ Figure 1A is a schematic of the 2DLP crystal, where the Pb–Br octahedra form the layers, connected through the ethylammonium chains. Mn²⁺ substitutes for Pb²⁺ in the planes. Figure 1B shows the morphological characteristic of the 2DLP using scanning electron microscopy (SEM), where folded and layered structures are observed, indicative of the 2D nature. Using energy dispersive spectroscopy (EDS) we further confirm the uniform and continuous distribution of Mn²⁺ throughout the 2DLP structure in Figure 1C. Room-temperature photoluminescence (PL) spectra (Figure S2) demonstrate efficient incorporation of Mn²⁺ dopants with strong emission centered around 610 nm from the d–d spin-forbidden transition of the 3d⁵ energy levels (⁴T → ⁶A), and

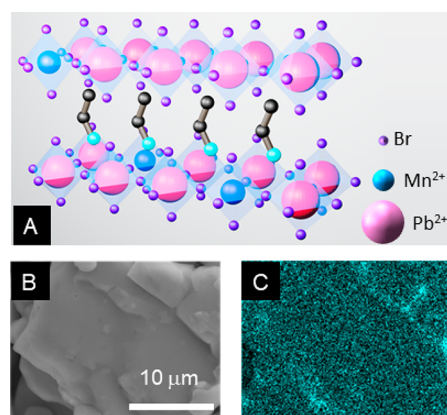


Figure 1. (A) Schematic of EA₂PbBr₄ with Mn²⁺ dopants substituting for Pb²⁺. (B) SEM image of EA₂PbBr₄:Mn²⁺. (C) EDS mapping of Mn²⁺ showing uniform dopant distribution within the SEM image.

as expected, no other emission is observed. The absence of any PL from the band edge confirms the uninhibited energy transfer between the host and the dopant ions. It is also interesting to note the absence of PL from STE states, an optical characteristic of undoped 2DLPs, is attributed²⁸ to an ET pathway between the 2DLP and the dopants occurring through the formation of intermediate trap sites on the picosecond scale.

PL emission between 20–100 K in two different samples with 2% and 7% doping are discussed next. Figure 2A is a map of the PL intensity of the 2% EA₂PbBr₄:Mn²⁺ sample, plotted

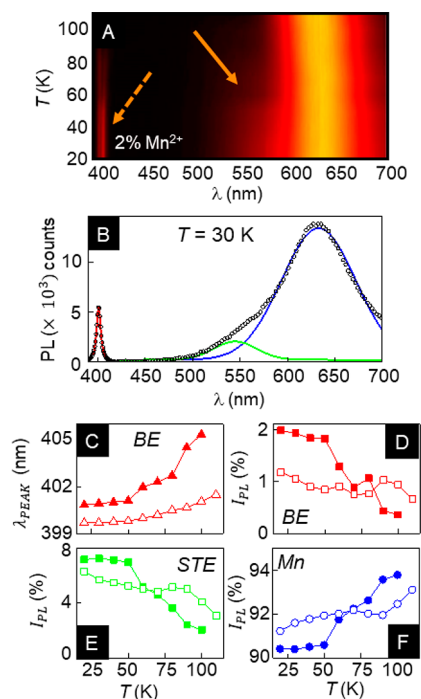


Figure 2. (A) PL intensity of 2% EA₂PbBr₄:Mn²⁺ mapped with emission wavelength and temperature. BE (dashed arrow) and STE emission (solid arrow) are visible in the map, along with the Mn²⁺ emission band centered at 630 nm. (B) PL spectrum at $T = 30$ K demonstrating the multiple peak fit used to characterize the emission. (C) BE emission peak wavelength and PL intensities of (D) BE, (E) STE, and (F) Mn²⁺ emission for 2% (solid symbols) and 7% Mn²⁺ doping (open symbols) plotted varying with T .

with temperature T and emission wavelength λ . The direct bandgap emission from excitonic recombination at the band edge (BE) is visible around 405 nm (dashed arrow). Between 20 and 100 K, a sideband emission in the region 550–600 nm is also observed (solid arrow), arising because of STE emission. This band disappears by $T \approx 100$ K for both doping concentrations (Figure S3) and does not re-emerge. The PL spectrum at $T = 30$ K in Figure 2B highlights the three distinct regions showing emission corresponding to the direct BE, the sideband from STEs and the Mn^{2+} dopants. Also shown are the fits to these separate bands from which we extract the emission peak λ_{PEAK} and the integrated intensity I_{PL} plotted in the following figures. In Figure 2C, λ_{PEAK} shows a red-shift with increasing T for both 2% (solid symbols) and 7% (hollow symbols) samples. In both the bulk and the low-dimensional variants OMHP emission typically blue-shifts with increasing T , arising from the “inverted” arrangements of the conduction and valence bands. For layered structures, spectral shift with T has been found to be dependent on the value of n , the number of inorganic layers between the organic cations, and red-shift is indicative of $n = 1$,¹⁸ which is also observed in the undoped sample (Figure S4). By comparison, Mn^{2+} emission red-shifts with decreasing T (Figures S5 and S6), which has been attributed to enhanced ligand field strength due to the contraction of the octahedra.³⁵ STE emission follows the same trend as Mn^{2+} in the doped samples, possibly because of the spectral overlap of the two bands.

The spectral shifts mostly confirm expected results, but the PL intensity I_{PL} of the BE, STE, and Mn^{2+} emission bands plotted in Figure 2D–F offers important insights into the ET pathways. Contributions from both BE and STE to I_{PL} decrease with increasing T , while that of Mn^{2+} concurrently increases. From this correlation, it is evident that the relative increase in the Mn dopant emission occurs through ET from both the STE band and directly from the BE. Consequently, we can model ET for $T < 100$ K as consisting of two pathways: (1) one allowing direct ET from the band edge to the Mn^{2+} band, and (2) the second allowing ET to the Mn^{2+} band through STEs. A simple representation of this is shown in Figure 3A, where k_1 denotes the transfer rate from the band edge to the STEs per excited charge carrier, k_2 the transfer rate constant from BE to the dopant energy levels, and k_3 the energy-transfer rate constant from the STE band to the dopants.

We can establish several relations between these rates, and we begin with the relaxation dynamics of the excited-state carriers in the BE using time-resolved photoluminescence (TRPL). The corresponding average lifetimes extracted using a double exponential fit to TRPL data (Figure S7A) is around ~ 230 ps for the entire range of $20 \text{ K} < T < 100 \text{ K}$ (Figure S7B). Such a short recombination lifetime is a result of the concurrent ET to the STE and Mn^{2+} energy bands.³⁶ The average recombination rate k_{Tot} between 20 and 100 K, determined from TRPL curves, is $43 \times 10^8 \text{ s}^{-1}$ and can be expressed as

$$k_{\text{Tot}} = k_{\text{exc}} + k_1 + k_2 \quad (1)$$

where k_{exc} is the direct recombination rate per exciton. Assuming negligible nonradiative recombination due to the high quantum efficiency in 2DLP, we obtain

$$k_1 N_{\text{BE}} - k_3 N_{\text{STE}} \propto N_{\text{STE}} \quad (2)$$

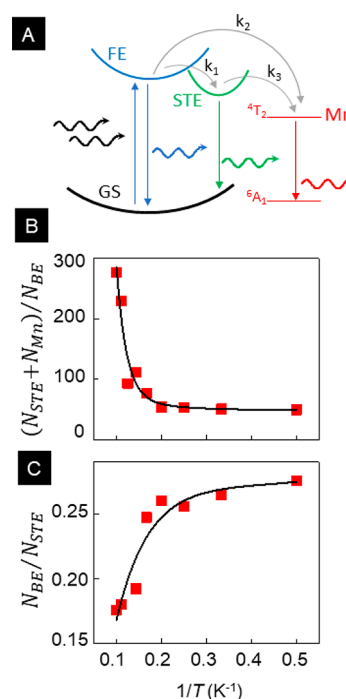


Figure 3. (A) Schematic representation of $\text{EA2PbBr}_4:\text{Mn}^{2+}$ energy bands. (B) Charge carrier densities N_{STE} and N_{Mn} normalized by N_{BE} plotted with $1/T$ for 2% $\text{Mn}^{2+}:\text{2DLP}$. (C) Ratio of N_{BE} and N_{STE} plotted as a function of $1/T$. Fits are explained in the text.

$$k_2 N_{\text{BE}} + k_3 N_{\text{STE}} \propto N_{\text{Mn}} \quad (3)$$

where N_{BE} , N_{STE} , and N_{Mn} represent the integrated charge carrier density of the BE, STE, and Mn bands, respectively. Solving the above

$$k_1 + k_2 \propto (N_{\text{STE}} + N_{\text{Mn}}) / N_{\text{BE}} \quad (4)$$

Following the same logic for energy transfer to Mn dopant from BE and STE, we get

$$k_1 N_{\text{BE}} = A N_{\text{STE}} + k_3 N_{\text{STE}} \quad (5)$$

Rearrangement of eq 5 leads to

$$\frac{A + k_3}{k_1} = \frac{N_{\text{BE}}}{N_{\text{STE}}} \quad (6)$$

We note that each of these rates can also be expressed using the well-known Arrhenius relations

$$k_{1,2,3} = a_{1,2,3} e^{-\Delta E_{1,2,3} / K_{\text{B}} T} \quad (7)$$

where $\Delta E_{1,2,3}$ is the activation energy corresponding to $k_{1,2,3}$, respectively, and K_{B} is the Boltzmann constant. Using the equivalence that the integrated charge carrier densities are proportional to the integrated PL intensities, we plot the ratios $(N_{\text{STE}} + N_{\text{Mn}}) / N_{\text{BE}}$ and $N_{\text{BE}} / N_{\text{STE}}$ with $1/T$ in Figure 3B,C and fit the data using eqs 3 and 5, respectively. From the fits we derive the activation energies for the various energy transfer routes. Their values are summarized in Table 1.

The activation energies ΔE_1 and ΔE_2 relate to ET from the BE, and given that the quantitative values correspond to thermal scales ≥ 100 K, it explains why we do not observe any changes in the excitonic recombination times over the range 20–100 K (Figure S7). Further, the same scale set by ΔE_1 is the reason why BE emission quenches around $T \approx 120$ K for

both doping levels, as seen in Figure 2D. Further confirmation that this activation energy is an intrinsic property of the 2DLP is obtained from a similar analysis of the undoped sample (Figure S8), where we calculate $\Delta E_1 = 4.7$ meV.

Comparing the activation values for the two different doping levels reveals additional insights. $\Delta E_2 \gg K_B T$ for not only the temperature range of these measurements but even at ambient temperatures, so we can conclude with certainty that there is negligible direct energy transfer from the BE to the dopants. This also explains why the ET time scale, as can be estimated from the BE TRPL data (Figure S7A,B) is known to not vary with increasing dopant concentration.²³ The main ET route is therefore from BE \rightarrow STE followed by STE \rightarrow Mn²⁺. In addition, ΔE_2 is lower for the sample with higher doping, while ΔE_1 increases. This possibly results in slightly larger proportion of direct ET from BE \rightarrow Mn²⁺, but these changes in activation energies are not large enough to make ET from BE \rightarrow Mn²⁺ the predominant pathway. Furthermore, the data in Figure 2D,E also show that the relative contributions of BE and STE to the total PL are smaller in the 7% sample to begin with and vary less with T , possibly because of the substantially low value of ΔE_3 in the 7% doped sample, which is comparable to the thermal energy even at temperatures as low as 20 K. These changes in the activation energy possibly arise from the larger distribution of trap states in the sample with larger doping owing to greater lattice distortion from the size mismatch between Pb and Mn ions, as well as from the higher density of doping-related defects states. The low energetic barriers to ET, both from and to the STEs (ΔE_1 and ΔE_3 raise the question of reverse energy and/or charge migration, and how those may affect the transfer rates. We note here that the ET model described here robustly takes this into account in the proportionality relation it is based on. All the states are in equilibrium under the condition of continuous illumination, as is the case for the ET measurements. Additional discussion is included in the Supporting Information.

Lastly, we focus on a different aspect of transition metal dopants such as Mn²⁺ in semiconductors beyond their roles related to luminescence. Strong sp–d exchange coupling between these discrete magnetic moments and the host carriers, particularly in quantum confined structures, allow magneto-optical modulations that can lead to magnetic polarons, giant Zeeman effect, and carrier-mediated ferromagnetism,^{37,38} which in turn drive applications ranging from spin-filtering³⁹ to magneto-optical gating⁴⁰ and quantum information processing.^{41,42} While most of these exciting properties have been investigated in II–VI and III–V materials, the high spin–orbit coupling (SOC) in some OMHPs indicates this class of compounds have considerable potential as candidates for similar phenomena,^{33,43} where strong SOC allows the bright host exciton with $\Delta J = \pm 1$ to populate the lowest spin state in Mn²⁺ ions.⁴⁴ Using polarization-resolved spectroscopy, we demonstrate spin-polarized Mn²⁺ emission in the absence of an external magnetic field in the 2DLPs.

Upon exciting the 2DLP using left circularly polarized light (designated σ^-) at 380 nm and analyzing the Mn²⁺ emission centered at 610 nm using circular polarization spectroscopy, we observe a 4% right circular polarization (σ^+) at $T = 80$ K, shown in Figure 4A. Note that the Mn²⁺ emission is polarized opposite to that of the excitation light. There are low dopant concentrations in these samples (2%–7%). The polarization value P_{Mn} drops to 2.4% by $T = 120$ K, plotted in Figure 4B, and the fact that it persists this far implies the ET rate is higher

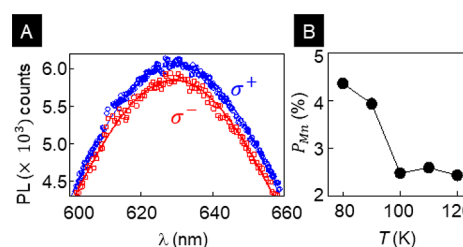


Figure 4. (A) Polarization-resolved Mn²⁺ emission at $T = 80$ K when excitation is σ^- polarized. (B) Degree of polarization P_{Mn} of Mn²⁺ emission as a function of T .

than the spin dephasing rate. The origin of this polarized emission is not the same as that in diluted magnetic semiconductor nanocrystals, where similar spin-polarized emission has been observed in a high magnetic field.³³ While the exact mechanism behind the spin-polarized emission of our samples is not fully understood yet, one possibility is the exchange interaction between the excited Mn²⁺ d-electron spins and optically injected sp-exciton spins. Theoretical studies have shown that off-diagonal terms in the sp–d exchange interaction term can facilitate simultaneous spin-flips and spin transfer in Mn-doped OMHPs.^{45,46} Further investigations following these initial results will undoubtedly allow insights into the detailed nature of these observations, particularly by using higher dopant concentrations. In 2DLPs in the limit of Mn²⁺ concentration less than 10%, no change of the dopant recombination dynamics has been observed with varying dopant content.^{28,47} This would indicate a lack of interactions between the dopant ions. However, in OMHP nanocrystals, Mn²⁺ concentration greater than $\sim 2\%$ leads to intrinsic magnetic behavior,³⁶ rooted in the inter-Mn²⁺ interactions. It would be of great interest to investigate the high dopant regime in 2DLPs, as the impact of both sp–d coupling between the host electrons and the dopants as well as dopant–dopant interactions would undoubtedly lead to modulation of spin and charge dynamics of both.

In conclusion, while doping is a very powerful tool for tuning functionalities in semiconductors, ranging from 3D to all other low-dimensional variants, OMHPs are relatively new entrants in this arena, and their properties are still in the process of being characterized to the full extent. In this context, our findings clarify significant aspects of energy transfer in doped 2D OMHP compounds, establishing the central role played by self-trapped excitons. STEs are clearly emissive at low temperatures and are the main route of ET from the band edge to the dopants, while there is almost no ET directly from the band edges to the Mn²⁺ ions, which is also supported by the relative magnitudes of the activation energies derived from spectral analysis. Varying the dopant concentration influences these energies and consequently enhances ET from STEs to the dopants. However, despite the negligible direct ET from the band edge excitons to Mn²⁺, the host–dopant exchange interaction is strong enough to allow optically polarizing the dopant spins via bandgap excitation. This is a most exciting observation, indicating the possibility of harnessing spin-charge couplings and tunable magneto-optical effects in OMHPs.

Synthesis. 2D single-layered EA₂PbBr₄ were synthesized via a grinding method. Typically, 0.40 mmol of EABr and 0.10 mmol of PbBr₂ were mixed and ground in an agate mortar and pestle under low humidity for more than 10 min. The resulting sample without the addition of Mn²⁺ was denoted by S-0 and

characterized directly without any modification. For 2D three-layered $\text{EA}_4\text{Pb}_3\text{Br}_{10}$ (denoted by T-0), the mole numbers of EABr and PbBr_2 were 0.1 and 0.40 mmol, respectively. The synthesis procedure was the same as that of 2D single-layered EA_2PbBr_4 . For the Mn-doped EA_2PbBr_4 series, the final molar ratio of $n_{\text{EA}\text{Br}}:(n_{\text{PbBr}_2} + n_{\text{MnBr}_2})$ was still kept at 4:1, but the molar feed ratio ($\text{PbBr}_2:\text{MnBr}_2$) was varied. For example, 2% Mn^{2+} -doped EA_2PbBr_4 was synthesized with 5% Mn^{2+} content, resulting in a 1:19 molar feed ratio (0.4:0.095:0.005 mmol EA:Pb:Mn).

PL. Excitation for PL measurements is provided by the frequency-doubled output of a Ti:sapphire laser (MIRA Duo, Coherent Inc.), tunable over the range 750–980 nm, and with a repetition rate of 76 MHz. The laser fundamental output is tuned to 760 nm, doubled to 380 nm using a barium beta borate (BBO) crystal. After collection, the emission is dispersed by a Princeton Scientific 250i spectrometer and then measured via a thermo-electrically cooled CCD, with a spectral resolution of 0.18 nm.

TRPL. For the time-resolved PL measurements, the signal is dispersed onto the spectrometer and then collected by a single-photon avalanche diode for analysis by a PicoQuant time-correlated single-photon counting system, with an instrument response function of 28 ps.

Temperature-Dependent Measurements. Temperature-dependent PL and TRPL was conducted using an Advanced Research Systems cryo-free, temperature-controlled cryostat. The sample was mounted on a stage in a vacuum chamber, and the temperature was varied from 20 to 300 K in 10 K steps. The temperature was increased starting at 20 K, and at each new set temperature 20 min of wait time was allocated for the sample to equilibrate prior to initiating data acquisition.

Polarization-Resolved Measurements. Circularly polarized excitation is generated using a linear polarizer and a quarter-wave plate in series, both rated in the UV spectral range. The emission is collected in reflection geometry and is investigated using a circular polarization analyzer, composed of a photoelastic modulator (PEM) (Hinds Instrument Inc., operating at $\lambda/4$) and a linear polarizer. After passing through the analyzer, the emission is focused onto a photodiode connected to a lock-in amplifier (Signal Recovery), working synchronously with the PEM. The voltage output of the lock-in at the reference frequency is proportional to $I_{\sigma^+} - I_{\sigma^-}$. Upon replacing the lock-in amplifier with a digital multimeter gives $I_{\sigma^+} + I_{\sigma^-}$ and dividing these two terms, the polarization (P) value of the emission is calculated.

ICP-OES Sample Preparation. To remove excess starting material after the grinding synthesis, as-prepared samples of pure EA_2PbBr_4 and Mn-doped EA_2PbBr_4 were washed several times in toluene via vacuum filtration. Approximately 2.5 mg of washed, dry samples were dissolved in 5 mL of a 1:1 5% glacial acetic acid and 3% hydrogen peroxide solution. Because of some remaining precipitate aggregation, this solution was thoroughly sonicated and mixed before the measurement to ensure solution homogeneity. Lead and manganese standards were prepared using 1:1 5% glacial acetic acid and 3% hydrogen peroxide solution as well.

ICP-OES Instrumentation. The Mn^{2+} doping concentrations of EA_2PbBr_4 were determined using a Thermo iCap 7400 radial view inductively coupled optical emissions spectrometer (ICP-OES). It uses an Echelle polychromator that enables rapid, simultaneous, multielement analysis. The RF forward

power was 1150 W. The wavelengths monitored were 220.353 nm for lead and 257.610 nm for manganese.

PXRD Instrumentation. PXRD was used to obtain the crystalline phase using a Rigaku America Miniflex powder diffractometer at University of California, Santa Cruz. The scanning angle range was 2° – 60° (2θ) with a rate of $20^\circ \text{ min}^{-1}$ and a 0.02° step size.

■ ASSOCIATED CONTENT

Supporting Information

The Supporting Information is available free of charge at <https://pubs.acs.org/doi/10.1021/acs.jpcllett.0c03287>.

- (1) Doping concentrations of Mn^{2+} obtained from ICP data;
- (2) PXRD of 2DLP with different Mn^{2+} dopant concentrations;
- (3) room-temperature PL spectra of doped 2DLP samples;
- (4) 2DLP mapped emission for 7% doped sample;
- (5) emission spectra and peak wavelength of undoped 2DLP at different temperatures;
- (6) peak emission wavelength shift for 2% doped sample;
- (7) peak emission wavelength shift for 7% doped sample;
- (8) time-resolved PL of 7% doped sample;
- (9) ratio of PL intensities of BE and STE emission of the undoped sample as a function of temperature;
- (10) verification of rate model robustness to reverse migration processes (PDF)

■ AUTHOR INFORMATION

Corresponding Authors

Jin Z. Zhang – Department of Chemistry and Biochemistry, University of California, Santa Cruz, California 95064, United States; orcid.org/0000-0003-3437-912X; Email: zhang@ucsc.edu

Sayantani Ghosh – Department of Physics, School of Natural Sciences, University of California, Merced, California 95343, United States; orcid.org/0000-0003-3440-7194; Email: sghosh@ucmerced.edu

Authors

Som Sarang – Department of Physics, School of Natural Sciences, University of California, Merced, California 95343, United States

William Delmas – Department of Physics, School of Natural Sciences, University of California, Merced, California 95343, United States; orcid.org/0000-0002-6030-0318

Sara Bonabi Naghadeh – Department of Chemistry and Biochemistry, University of California, Santa Cruz, California 95064, United States

Vivien Cherrette – Department of Chemistry and Biochemistry, University of California, Santa Cruz, California 95064, United States

Complete contact information is available at: <https://pubs.acs.org/doi/10.1021/acs.jpcllett.0c03287>

Author Contributions

S.S. performed all measurements and led data analysis efforts. S.B.N. and V.C. synthesized all samples. W.D. assisted in analysis and figure creation. J.Z.Z. and S.G. supervised all characterization and measurements.

Notes

The authors declare no competing financial interest.

ACKNOWLEDGMENTS

This work was possible through the support of NASA MIRO award NNX15AQ01A. We are grateful to Binbin Luo for first introducing to us the method of synthesis to make all the samples studied in this work.

ABBREVIATIONS

EA ₂ PbBr ₄ :Mn ²⁺	Mn ²⁺ doped ethylammonium lead bromide
2DLP	two-dimensional layered perovskite
PL	photoluminescence
BE	band-edge
STE	self-trapped exciton
ET	energy transfer
OMHP	organometal halide perovskite
PQDs	perovskite quantum dots
2DLPs	two-dimensional layered perovskites
LEDs	light-emitting devices
EDS	energy dispersive spectroscopy
TRPL	time-resolved photoluminescence
SOC	spin-orbit coupling

REFERENCES

- (1) Jena, A. K.; Kulkarni, A.; Miyasaka, T. Halide Perovskite Photovoltaics: Background, Status, and Future Prospects. *Chem. Rev.* **2019**, *119* (5), 3036–3103.
- (2) NREL. Best Research-Cell Efficiency Chart Photovoltaic Research. <https://www.nrel.gov/pv/cell-efficiency.html> (accessed 2019-08-05).
- (3) Zhang, M.; Zhang, F.; Wang, Y.; Zhu, L.; Hu, Y.; Lou, Z.; Hou, Y.; Teng, F. High-Performance Photodiode-Type Photodetectors Based on Polycrystalline Formamidinium Lead Iodide Perovskite Thin Films. *Sci. Rep.* **2018**, *8* (1), 11157.
- (4) Yakunin, S.; Protesescu, L.; Krieg, F.; Bodnarchuk, M. I.; Nedelcu, G.; Humer, M.; De Luca, G.; Fiebig, M.; Heiss, W.; Kovalenko, M. V. Low-Threshold Amplified Spontaneous Emission and Lasing from Colloidal Nanocrystals of Cesium Lead Halide Perovskites. *Nat. Commun.* **2015**, *6* (1), 8056.
- (5) Gao, Y.; Wang, S.; Huang, C.; Yi, N.; Wang, K.; Xiao, S.; Song, Q. Room Temperature Three-Photon Pumped CH₃NH₃PbBr₃ Perovskite Microlasers. *Sci. Rep.* **2017**, *7* (1), 45391.
- (6) Song, T.-B.; Yokoyama, T.; Stoumpos, C. C.; Logsdon, J.; Cao, D. H.; Wasielewski, M. R.; Aramaki, S.; Kanatzidis, M. G. Importance of Reducing Vapor Atmosphere in the Fabrication of Tin-Based Perovskite Solar Cells. *J. Am. Chem. Soc.* **2017**, *139* (2), 836–842.
- (7) Li, Y.; Yan, W.; Li, Y.; Wang, S.; Wang, W.; Bian, Z.; Xiao, L.; Gong, Q. Direct Observation of Long Electron-Hole Diffusion Distance in CH₃NH₃PbI₃ Perovskite Thin Film. *Sci. Rep.* **2015**, *5* (1), 14485.
- (8) Huang, Y.; Liu, J.; Deng, Y.; Qian, Y.; Jia, X.; Ma, M.; Yang, C.; Liu, K.; Wang, Z.; Qu, S.; Wang, Z. The Application of Perovskite Materials in Solar Water Splitting. *J. Semicond.* **2020**, *41* (1), 011701.
- (9) Sarang, S.; Bonabi Naghadeh, S.; Luo, B.; Kumar, P.; Betady, E.; Tung, V.; Scheibner, M.; Zhang, J. Z.; Ghosh, S. Stabilization of the Cubic Crystalline Phase in Organometal Halide Perovskite Quantum Dots via Surface Energy Manipulation. *J. Phys. Chem. Lett.* **2017**, *8* (21), 5378–5384.
- (10) Naghadeh, S. B.; Sarang, S.; Brewer, A.; Allen, A.; Chiu, Y. H.; Hsu, Y. J.; Wu, J. Y.; Ghosh, S.; Zhang, J. Z. Size and Temperature Dependence of Photoluminescence of Hybrid Perovskite Nanocrystals. *J. Chem. Phys.* **2019**, *151* (15), 154705.
- (11) Protesescu, L.; Yakunin, S.; Bodnarchuk, M. I.; Krieg, F.; Caputo, R.; Hendon, C. H.; Yang, R. X.; Walsh, A.; Kovalenko, M. V. Nanocrystals of Cesium Lead Halide Perovskites (CsPbX₃, X = Cl, Br, and I): Novel Optoelectronic Materials Showing Bright Emission with Wide Color Gamut. *Nano Lett.* **2015**, *15* (6), 3692–3696.
- (12) Vickers, E. T.; Enlow, E. E.; Delmas, W. G.; DiBenedetto, A. C.; Chowdhury, A. H.; Bahrami, B.; Dreskin, B. W.; Graham, T. A.; Hernandez, I. N.; Carter, S. A.; et al. Enhancing Charge Carrier Delocalization in Perovskite Quantum Dot Solids with Energetically Aligned Conjugated Capping Ligands. *ACS Energy Lett.* **2020**, *5* (3), 817–825.
- (13) Utzat, H.; Sun, W.; Kaplan, A. E. K.; Krieg, F.; Ginterseder, M.; Spokoiny, B.; Klein, N. D.; Shulenberger, K. E.; Perkinson, C. F.; Kovalenko, M. V.; et al. Coherent Single-Photon Emission from Colloidal Lead Halide Perovskite Quantum Dots. *Science* **2019**, *363* (6431), 1068–1072.
- (14) Park, Y. S.; Guo, S.; Makarov, N. S.; Klimov, V. I. Room Temperature Single-Photon Emission from Individual Perovskite Quantum Dots. *ACS Nano* **2015**, *9* (10), 10386–10393.
- (15) Cortecchia, D.; Neutzner, S.; Kandada, A. R. S.; Mosconi, E.; Meggiolaro, D.; De Angelis, F.; Soci, C.; Petrozza, A. Broadband Emission in Two-Dimensional Hybrid Perovskites: The Role of Structural Deformation. *J. Am. Chem. Soc.* **2017**, *139* (1), 39–42.
- (16) Thirumal, K.; Chong, W. K.; Xie, W.; Ganguly, R.; Muduli, S. K.; Sherburne, M.; Asta, M.; Mhaisalkar, S.; Sum, T. C.; Soo, H. Sen; et al. Morphology-Independent Stable White-Light Emission from Self-Assembled Two-Dimensional Perovskites Driven by Strong Exciton-Phonon Coupling to the Organic Framework. *Chem. Mater.* **2017**, *29* (9), 3947–3953.
- (17) Chen, Y.; Sun, Y.; Peng, J.; Tang, J.; Zheng, K.; Liang, Z. 2D Ruddlesden-Popper Perovskites for Optoelectronics. *Adv. Mater.* **2018**, *30* (2), 1703487.
- (18) Long, H.; Peng, X.; Lu, J.; Lin, K.; Xie, L.; Zhang, B.; Ying, L.; Wei, Z. Exciton-Phonon Interaction in Quasi-Two Dimensional Layered (PEA)₂(CsPbBr₃):N₋₁PbBr₄ Perovskite. *Nanoscale* **2019**, *11* (45), 21867–21871.
- (19) Li, S.; Luo, J.; Liu, J.; Tang, J. Self-Trapped Excitons in All-Inorganic Halide Perovskites: Fundamentals, Status, and Potential Applications. *J. Phys. Chem. Lett.* **2019**, *10* (8), 1999–2007.
- (20) Li, S.; Hu, Q.; Luo, J.; Jin, T.; Liu, J.; Li, J.; Tan, Z.; Han, Y.; Zheng, Z.; Zhai, T.; et al. Self-Trapped Exciton to Dopant Energy Transfer in Rare Earth Doped Lead-Free Double Perovskite. *Adv. Opt. Mater.* **2019**, *7* (23), 1901098.
- (21) Mir, W. J.; Jagadeeswararao, M.; Das, S.; Nag, A. Colloidal Mn-Doped Cesium Lead Halide Perovskite Nanoplatelets. *ACS Energy Lett.* **2017**, *2* (3), 537–543.
- (22) Zhang, L.; Jiang, T.; Yi, C.; Wu, J.; Liu, X. K.; He, Y.; Miao, Y.; Zhang, Y.; Zhang, H.; Xie, X.; et al. Bright Free Exciton Electroluminescence from Mn-Doped Two-Dimensional Layered Perovskites. *J. Phys. Chem. Lett.* **2019**, *10* (11), 3171–3175.
- (23) Biswas, A.; Bakthavatsalam, R.; Kundu, J. Efficient Exciton to Dopant Energy Transfer in Mn²⁺-Doped (C₄H₉NH₃)₂PbBr₄ Two-Dimensional (2D) Layered Perovskites. *Chem. Mater.* **2017**, *29* (18), 7816–7825.
- (24) Das Adhikari, S.; Dutta, S. K.; Dutta, A.; Guria, A. K.; Pradhan, N. Chemically Tailoring the Dopant Emission in Manganese-Doped CsPbCl₃ Perovskite Nanocrystals. *Angew. Chem.* **2017**, *129* (30), 8872–8876.
- (25) Sun, C.; Gao, Z.; Deng, Y.; Liu, H.; Wang, L.; Su, S.; Li, P.; Li, H.; Zhang, Z.; Bi, W. Orange to Red, Emission-Tunable Mn-Doped Two-Dimensional Perovskites with High Luminescence and Stability. *ACS Appl. Mater. Interfaces* **2019**, *11* (37), 34109–34116.
- (26) Zhou, G.; Jiang, X.; Molokeev, M.; Lin, Z.; Zhao, J.; Wang, J.; Xia, Z. Optically Modulated Ultra-Broad-Band Warm White Emission in Mn²⁺-Doped (C₆H₁₈N₃O₂)PbBr₄ Hybrid Metal Halide Phosphor. *Chem. Mater.* **2019**, *31* (15), 5788–5795.
- (27) Zhu, J.; Yang, X.; Zhu, Y.; Wang, Y.; Cai, J.; Shen, J.; Sun, L.; Li, C. Room-Temperature Synthesis of Mn-Doped Cesium Lead Halide Quantum Dots with High Mn Substitution Ratio. *J. Phys. Chem. Lett.* **2017**, *8* (17), 4167–4171.
- (28) Luo, B.; Guo, Y.; Li, X.; Xiao, Y.; Huang, X.; Zhang, J. Z. Efficient Trap-Mediated Mn²⁺ Dopant Emission in Two Dimensional Single-Layered Perovskite (CH₃CH₂NH₃)₂PbBr₄. *J. Phys. Chem. C* **2019**, *123* (23), 14239–14245.

- (29) Bakthavatsalam, R.; Biswas, A.; Chakali, M.; Bangal, P. R.; Kore, B. P.; Kundu, J. Temperature-Dependent Photoluminescence and Energy-Transfer Dynamics in Mn^{2+} -Doped $(\text{C}_4\text{H}_9\text{NH}_3)_2\text{PbBr}_4$ Two-Dimensional (2D) Layered Perovskite. *J. Phys. Chem. C* **2019**, *123* (8), 4739–4748.
- (30) Hou, L.; Zhu, Y.; Zhu, J.; Gong, Y.; Li, C. Mn-Doped 2D Sn-Based Perovskites with Energy Transfer from Self-Trapped Excitons to Dopants for Warm White Light-Emitting Diodes. *J. Mater. Chem. C* **2020**, *8* (25), 8502–8506.
- (31) Goryca, M.; Kazimierczuk, T.; Nawrocki, M.; Golnik, A.; Gaj, J. A.; Kossacki, P.; Wojnar, P.; Karczewski, G. Optical Manipulation of a Single Mn Spin in a CdTe-Based Quantum Dot. *Phys. Rev. Lett.* **2009**, *103* (8), 087401.
- (32) Le Gall, C.; Besombes, L.; Boukari, H.; Kolodka, R.; Cibert, J.; Mariette, H. Optical Spin Orientation of a Single Manganese Atom in a Semiconductor Quantum Dot Using Quasiresonant Photoexcitation. *Phys. Rev. Lett.* **2009**, *102* (12), 127402.
- (33) Viswanatha, R.; Pietryga, J. M.; Klimov, V. I.; Crooker, S. A. Spin-Polarized Mn^{2+} Emission from Mn-Doped Colloidal Nanocrystals. *Phys. Rev. Lett.* **2011**, *107* (6), 067402.
- (34) Besombes, L.; Leger, Y.; Maingault, L.; Ferrand, D.; Mariette, H.; Cibert, J. Carrier-Induced Spin Splitting of an Individual Magnetic Atom Embedded in a Quantum Dot. *Phys. Rev. B: Condens. Matter Mater. Phys.* **2005**, *71* (16), 161307.
- (35) Nag, A.; Cherian, R.; Mahadevan, P.; Gopal, A. V.; Hazarika, A.; Mohan, A.; Vengurlekar, A. S.; Sarma, D. D. Size-Dependent Tuning of Mn^{2+} Emission in Mn^{2+} -Doped CdS Nanocrystals: Bulk vs Surface. *J. Phys. Chem. C* **2010**, *114* (43), 18323–18329.
- (36) De, A.; Mondal, N.; Samanta, A. Luminescence tuning and exciton dynamics of Mn-doped CsPbCl_3 nanocrystals. *Nanoscale* **2017**, *9*, 16722.
- (37) Beaulac, R.; Archer, P. I.; Ochsenein, S. T.; Gamelin, D. R. Mn^{2+} -Doped CdSe Quantum Dots: New Inorganic Materials for Spin-Electronics and Spin-Photonics. *Adv. Funct. Mater.* **2008**, *18* (24), 3873–3891.
- (38) Besombes, L.; Léger, Y.; Maingault, L.; Ferrand, D.; Mariette, H.; Cibert, J. Probing the Spin State of a Single Magnetic Ion in an Individual Quantum Dot. *Phys. Rev. Lett.* **2004**, *93* (20), 207403.
- (39) Efros, A. L.; Rashba, E. I.; Rosen, M. Paramagnetic Ion-Doped Nanocrystal as a Voltage-Controlled Spin Filter. *Phys. Rev. Lett.* **2001**, *87* (20), 206601.
- (40) *Magneto-Optics*; Sugano, S., Kojima, N., Eds.; Springer-Verlag: Berlin, 2000.
- (41) Fernández-Rossier, J.; Brey, L. Ferromagnetism Mediated by Few Electrons in a Semimagnetic Quantum Dot. *Phys. Rev. Lett.* **2004**, *93* (11), 117201.
- (42) Qu, F.; Hawrylak, P. Magnetic Exchange Interactions in Quantum Dots Containing Electrons and Magnetic Ions. *Phys. Rev. Lett.* **2005**, *95* (21), 217206.
- (43) Wang, J.; Zhang, C.; Liu, H.; McLaughlin, R.; Zhai, Y.; Vardeny, S. R.; Liu, X.; McGill, S.; Semenov, D.; Guo, H.; Tsuchikawa; Vardeny, Z. V.; et al. Spin-Optoelectronic Devices Based on Hybrid Organic-Inorganic Trihalide Perovskites. *Nat. Commun.* **2019**, *10* (1), 129.
- (44) Chernenko, A. V.; Brichkin, A. S.; Sobolev, N. A.; Carmo, M. C. Mechanisms of Manganese-Assisted Non-Radiative Recombination in Cd(Mn)Se/Zn(Mn)Se Quantum Dots. *J. Phys.: Condens. Matter* **2010**, *22* (35), 355306.
- (45) Léger, Y.; Besombes, L.; Maingault, L.; Mariette, H. Valence-Band Mixing in Neutral, Charged, and Mn-Doped Self-Assembled Quantum Dots. *Phys. Rev. B: Condens. Matter Mater. Phys.* **2007**, *76* (4), 045331.
- (46) Le Gall, C.; Besombes, L.; Boukari, H.; Kolodka, R.; Cibert, J.; Mariette, H. Optical Spin Orientation of a Single Manganese Atom in a Semiconductor Quantum Dot Using Quasiresonant Photoexcitation. *Phys. Rev. Lett.* **2009**, *102* (12), 127402.
- (47) Dutta, S. K.; Dutta, S. A.; Das Adhikari, S.; Pradhan, N. Doping Mn^{2+} in Single-Crystalline Layered Perovskite Microcrystals. *ACS Energy Lett.* **2019**, *4*, 343.